International Journal of
Scientific Research in Science and Technology (IJSRST)
Print ISSN : 2395-6011, Online ISSN : 2395-602X
International Conference on Advanced Materials
Held on 14, 15 December 2017, Organized by Department of Physics,
St. Joseph's College, Trichy, Tamilnadu, India

Effect of Mg Substitution on the Structural, Magnetic and Hyperfine Properties of $ZnFe_2O_4$ Nanopowders Synthesized by Spray Pyrolysis Method

Subin P. John, Jacob Mathew*
Mossbauer Research group, St. Berchmans Autonomous College, Kerala, India.
*Corresponding author: e-mail- jacob.chrisdale@gmail.com

Abstract

$Mg_xZn_{1-x}Fe_2O_4$ nanoparticles were synthesized by spray pyrolysis method using polymer precursor and characterized their structural, magnetic and hyperfine properties as a function of magnesium concentration. X-ray diffraction revealed cubic spinel structure of the prepared samples and structural refinement was done by Rietveld method. Cation distribution obtained from the Rietveld method reflected migration of cations among the interstitial sites. Fourier transform infrared spectroscopy confirmed the formation of spinel structure of the nanoparticles and shift of band center with magnesium doping due to cation migration was observed. Saturation magnetization increased with magnesium concentration due to enhancement in A-B superexchange interaction and coercivity varied in accordance with Brown's relation. The curve fitting of the magnetization data revealed coexistence of superparamgnetic, paramagnetic and ferromagnetic phases in the prepared nanoparticles. Mossbauer spectroscopy, a technique with different operating time scale than that of vibration sample magnetometer, indicated incomplete magnetic ordering and strongly confirmed the enhancement of A-B interaction with magnesium concentration. The Mossbauer studies further confirmed the coexistence of different magnetic phases in the sample.

Keywords: Mg-Zn nanoferrites, Cation migration, A-B super exchange interaction, Superparamagnetism, Coexistence of magnetic phases, Mossbauer spectroscopy

1. Introduction

Ferrites have wide range of technological applications owing to their unique electric and magnetic properties in the fields of high-frequency devices, magnetic fluids, microwaves, magnetic data storage, biomedical applications, magnetic resonance imaging and gas sensors. Ferrites in nanoscale exhibit improved physical, chemical and magnetic properties and are recently used for developing nanosized devices in biomedical field [1,2]. The cubic spinel ferrite with general formula $MeFe_2O_4$ (Me = Fe, Co, Ni, Mn, Mg, Zn...) belongs to space group $Fd\bar{3}m$. Unit cell of spinel ferrites has eight molecules of $MeFe_2O_4$ and oxygen ions forms a face centered cubic (f c c) lattice. In this structure two kinds of interstitial sites occur, the tetrahedral (A) and octahedral (B) sites which are surrounded by four and six oxygen ions respectively [3].

Superparamagnetic (SPM) nanoparticles–a new genre of magnetic particles-have recently shown rapid advance in the field of magnetic hyperthermia because of high level of heat generation, non-retainment of magnetization after the removal of applied magnetic field, easy targeting, suitability for human body magnetic fields and easy circulation through capillaries without agglomeration. Among many nanospinel ferrites that exhibit SPM properties and having potential for application in magnetic hyperthermia, Mg-Zn ferrite turns out to be a promising candidate due to their inhibitory nature on cancer cell growth. Moreover the Mg-Zn ferrites have the capability of fine tuning its magnetic properties to desirable values by controlling the doping concentrations of cations [4]. Doping of Mg^{2+} in zinc ferrite, can induce hopping of ions between the tetrahedral and octahedral sites. As the ions at the A and B sites greatly control the properties of ferrites, the gradual substitution of Mg^{2+} can vary the structural and magnetic properties to desired values. In this paper, we report the cost effective synthesis of Mg-Zn ferrite nanoparticles by polymer assisted spray pyrolysis method and the effect of magnesium substitution on structural and magnetic properties of zinc ferrite. We investigated the magnetic and hyperfine properties using vibration sample magnetometer and Mossbauer spectroscopy having different operating time scales and the analysis observed a coexistence of superparamagnetic, ferrimagnetic and paramagnetic phases in the prepared Mg-Zn ferrite nanoparticles.

2. Experimental

Magnesium doped zinc ferrite nanoparticles with formula $Mg_xZn_{1-x}Fe_2O_4$ (where x = 0.1, 0.2, 0.3, 0.4 and 0.5) were synthesized by spray pyrolysis method. The starting materials: magnesium nitrate ($Mg(NO_3)_2 6H_2O$, Merck GR), zinc nitrate ($Zn(NO_3)_2.6H_2O$, Merck LR) and ferric nitrate ($Fe(NO_3)_3.\ 6H_2O$, Himedia AR) were dissolved in double distilled water in accordance with doping concentrations. These nitrate solutions were added to 2 wt% polyvinyl alcohol (PVA, Loba Chemie, LR) and stirred continuously until the solution became homogenous. The solution was transferred to a spray gun and sprayed to a glass plate in spray pyrolysis unit kept at 130˚C. When sprayed solution became a geliish layer, the glass plate was taken out and cooled. Sample layer on the glass plate was peeled off and calcinated at 450˚C to obtain magnesium zinc ferrite nanoparticles.

The x-ray diffraction (XRD) analysis of the samples was done with PANlytical X'Pert-PRO X-ray diffractometer using Cu-Kα radiations (λ = 1.54060 Å). The morphological analysis was done by transmission electron microscopy (TEM) (Jeol/JEM 2100) operated at 200 kV. Fourier transform infrared spectroscopy (FTIR) of the samples was recorded using Thermo Nicolet, Avatar 370 spectrometer in the range 400-4000 cm^{-1} at a resolution of 4 cm^{-1}. The variation of magnetization with applied magnetic field in the range 0 - 15,000 Oe at room temperature was studied using a Lakeshore 7410 vibration sample magnetometer (VSM). Fe^{57} Mossbauer measurements were carried out at room temperature in transmission mode with a $^{57}Co/Rh$ radioactive source in constant acceleration mode using a standard personal computer based Mossbauer spectrometer.

3. Results and Discussion

3.1. X-ray diffraction studies

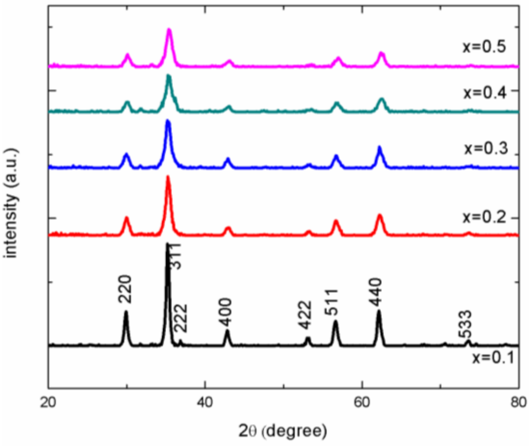

Figure 1. XRD patterns of $Mg_xZn_{1-x}Fe_2O_4$ nanoparticles

The structural analysis of $Mg_xZn_{1-x}Fe_2O_4$ (x = 0.1, 0.2, 0. 3, 0.4 and 0.5) nanoparticles was performed using x-ray diffraction technique. The XRD patterns are shown in Figure 1 were indexed by Bragg law. The presence of (220), (311), (222), (400), (422), (511) and (440) planes with most intense (311) reflection in the XRD pattern revealed the face centered cubic spinel structure of the samples. It is also evident from the Figure 1 that all the peaks are intense and broadening of the peaks are attributed to nonideal Bragg reflection occurring in nanoparticles. Structural refinement of the nanoferrites was done by Rietveld method using FULLPROFF program and refinement pattern is shown in Figure 2. The refinement was started using the space group $Fd\bar{3}m$ in which the oxygen anions occupy wyckoff position 32e with coordinates (0.25, 0.25, 0.25), tetrahedral sites at 8f with coordinates (0.125, 0.125, 0.125) and octahedral sites occupy 16c positions with coordinates (0.5, 0.5, 0.5). The Rietveld method was performed refining scale coefficient, background, instrumental parameters, cell parameters, full width half maximum (FWHM) parameters, isothermal parameters, atomic positions, occupancy and shape parameters in sequence mode. The background was modeled with six coefficient polynomial function and the experimental profile with Thompson-Cox-Hastings pseudo-Voight function [5]. The cation distribution of the samples by the Rietveld refinement is shown in Table 1, where the ions on the tetrahedral sites are given in front of the square brackets and the octahedral ions between the brackets. Also the lattice constant and the oxygen position parameter obtained from the Rietveld method is listed in Table 2. The crystallite size was determined using Scherrer equation. The x-ray density defined as the weight of atoms in unit cell per volume of unit cell were calculated by the formula

$$D_x = \frac{8M}{Na^3} \qquad \text{... (1)}$$

where N is Avagadro's number (= 6.0225 x 10^{23} atom/mole), M is the molecular weight of the sample, 'a' is the lattice constant and the factor '8' represents number of molecules in the unit cell. We have, further, calculated lattice strain using the modified Williamson and Hall equation

$$\eta = \frac{2d\left|K-1\right|}{D} \qquad \text{... (2)}$$

where d is the lattice spacing for (311) planes, K(0.89) is the shape factor and D is the average crystallite size [6]. The variation of lattice constant and x-ray density is shown in Figure 2.

The crystallite size obtained from Scherrer formula lies in the range 10.28-16.83 nm, indicating that the prepared samples are in the nano reigm and Mg doping in zinc ferrite has not considerable size effect. Zinc ferrite has a normal spinel structure in which Zn^{2+} and Fe^{3+} ions occupying tetrahedral (A) and octahedral (B) sites respectively [7]. When Mg^{2+} ions, a B site specific diamagnetic cation was doped in zinc ferrite, it might initiate migration of Fe^{3+} ions to A sites. This is possible since number of A site vacancies are enhanced due to reduction in A site specific zinc cations [8]. From the Table 1, although Mg^{2+} and Zn^{2+} have strong preferences to octahedral and tetrahedral sites respectively, they occupy the other sites in small amount. The Fe^{3+} ions migrate from octahedral to tetrahedral site with the increase of magnesium concentration. The lattice constant decreased with magnesium concentration owing to replacement of cations with larger ionic radius (Zn = 0.82 Å) by cation with smaller ionic radius in accordance with Vegard's law [9]. Even though lattice constant decreased with magnesium concentration, the x-ray density also followed same trend and this is due to the fact that reduction in molecular weight is greater than the decrease of volume of unit cell (Figure 3) [10].

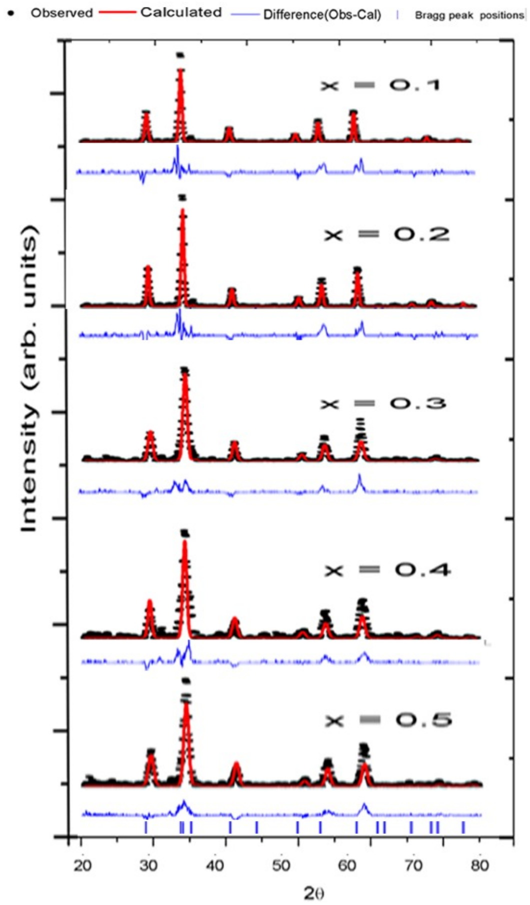

Figure 2. Rietveld refined XRD patterns of $Mg_xZn_{1-x}Fe_2O_4$ nanoferrites

Table 1. Cation distribution of the nanoferrites

Chemical Formula	Cation Distribution
$Mg_{0.1}Zn_{0.9}Fe_2O_4$	$Mg_{0.02}Zn_{0.77}Fe_{0.01}[Mg_{0.08}Zn_{0.13}Fe_{1.99}]O_4$
$Mg_{0.2}Zn_{0.8}Fe_2O_4$	$Mg_{0.06}Zn_{0\cdot67}Fe_{0.06}[Mg_{0.14}Zn_{0.13}Fe_{1.94}]O_4$
$Mg_{0.3}Zn_{0.7}Fe_2O_4$	$Mg_{0.09}Zn_{0\cdot65}Fe_{0.04}[Mg_{0.21}Zn_{0.05}Fe_{1.96}]O_4$
$Mg_{0.4}Zn_{0.6}Fe_2O_4$	$Mg_{0.12}Zn_{0\cdot48}Fe_{0.12}[Mg_{0.28}Zn_{0.12}Fe_{1.88}]O_4$
$Mg_{0.5}Zn_{0.5}Fe_2O_4$	$Mg_{0.17}Zn_{0\cdot45}Fe_{0.19}[Mg_{0.33}Zn_{0.05}Fe_{1.81}]O_4$

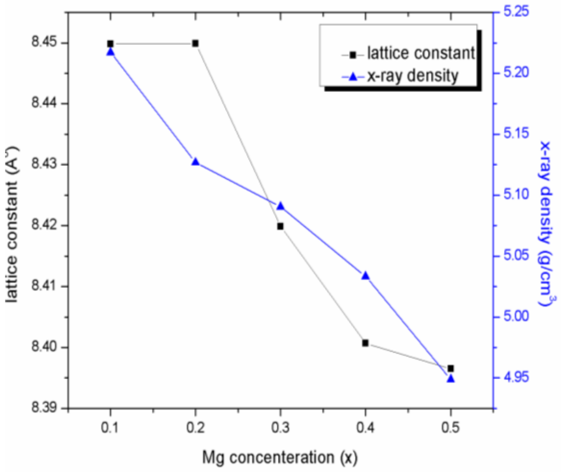

Figure 3. Lattice parameter and x-ray density as a function of Mg content in $Mg_xZn_{1-x}Fe_2O_4$ system

Table 2. Structural parameters of $Mg_xZn_{1-x}Fe_2O_4$ system

Magnesium Concentration (x)	Crystallite Size (nm)	Strain (η)	Lattice Constant (Å)	Oxygen Parmeter (u)	x-ray density (g/cm^3)
0.1	16.8384	0.0024	8.4498	0.2539	5.2173
0.2	12.803	0.0044	8.4499	0.2545	5.1269
0.3	13.7566	0.0044	8.4199	0.25635	5.0905
0.4	10.2860	0.0070	8.4007	0.2600	5.0334
0.5	11.2249	0.0052	8.3965	0.2622	4.9489

3.2. Transmission Electron Microscopy Studies

The TEM image of $Mg_{0.5}Zn_{0.5}Fe_2O_4$ is shown in Figure 4 and the majority of particles have spherical morphology. The average particle size obtained was about 15 nm and particle size ranges from 9-19 nm as shown in the histogram. The TEM image of $Mg_{0.5}Zn_{0.5}Fe_2O_4$ is shown in Figure 4 and the majority of particles have spherical morphology. The average particle size obtained was about 15 nm and particle size ranges from 9-19 nm as shown in the histogram.The particle size distribution suggest a possibility of coexistence of small superparamagnetic particles and some bigger particles [11]. The particle size obtained from TEM is nearly equal to the cryatallite determined from Scherrer formula indictes that the entire particle is a single crystallite. The selected area electron diffraction (SAED) pattern emphasis on the polycrystalline nature of the sample[12]. Inter planar distance of (311) plane from TEM image (2.50 Å) is in good agreement with XRD data (2.53 Å). The slight agglomoration of the particles is due to magnetic nature of samples. [13, 14].

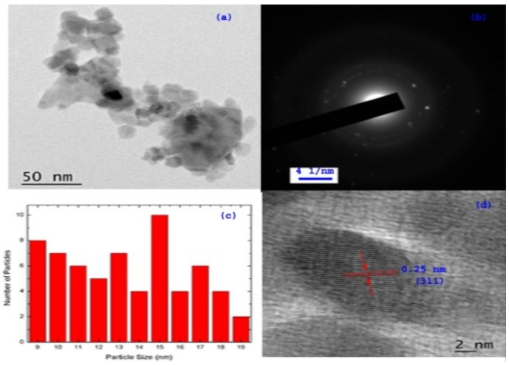

Figure 4. (a) TEM micrograph, (b) SAED pattern, (c) histogram of particle size and (d) interplanar spacing of $Mg_{0.5}Zn_{0.5}Fe_2O_4$ nanoparticles

3.3. Fourier transform infrared spectroscopy studies

FTIR spectra of the $Mg_xZn_{1-x}Fe_2O_4$ nanoparticles are presented in Figure 5. There exist two metal–oxygen bands in the FTIR spectra of spinel ferrites by the band vibration of metals at the tetrahedral and octahedral sites with the oxygen. The ν_1 band formed by the intrinsic stretching vibration of metal at tetrahedral sites with oxygen is observed in the range 500 - 600 cm^{-1}and the ν_2 band formed by the intrinsic stretching vibration of metal at octahedral site is observed in the range 385- 430 cm^{-1}[15]. The centre of the ν_1 band shifted to higher wavenumber with magnesium concentration and the shift is because of the migration of Fe^{3+} ions from octahedral to tetrahedral sites replacing Zn^{2+} as in the Table 1. Since stretching wavenumber is inversely proportional to atomic weight, the increasing content of comparatively lighter Fe^{3+} at tetrahedral sites replacing Zn^{2+} may be attributed to shift in ν_1 band to higher values. As there is no splitting or shoulders in the ν_1 band, presence of Fe^{2+} at the A site can be ruled out[16]. Since the detection limit of FTIR instrument was above 400 cm^{-1}, the ν_2 band was not detected[17]. The bands at 1400-1700 and 2925-2810 cm^{-1} were assigned to carboxyl group (COO^-) and stretching of C-H bonds respectively. The broad band centered at 3430 cm^{-1} is attributed to hydrogen bonded O-H groups arising from surface hydroxyl groups on nanoparticles and adsorbed water [18].

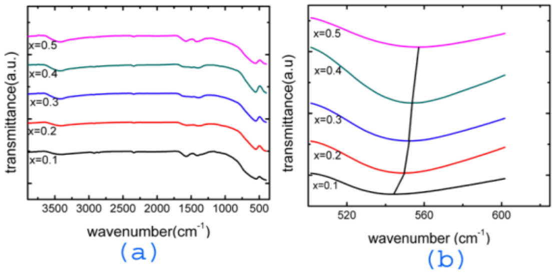

Figure 5. (a) FTIR spectra of $Mg_xZn_{1-x}Fe_2O_4$ nanoparticles and (b) enlarged ν_1 band

3.4. Magnetic Studies

Variation of magnetization of $Mg_xZn_{1-x}Fe_2O_4$ nanoparticles with applied field at room temperature measured by VSM is shown in Figure 6. Magnetic parameters: saturation magnetization (M_s), magnetic moment per formula unit (η_B), coercivity (H_c), retentivity (Mr) and squareness ratio (M_r / M_s) of the nanoparticles are tabulated in Table 3 and plotted in Fig 7. The magnetic moment per formula unit in Bohr magnetons is obtained from the equation,

$$\eta_B = \frac{MW \times M_s}{5585} \qquad \text{... (4)}$$

where MW is the molecular weight and M_s is the saturation magnetization in emu/g. The magnetocrystalline anisotropy constant (K_1) was estimated using Brown's relation

$$H_c = \frac{2K_1}{M_s} \qquad \text{... (5)}$$

where M_s is the saturation magnetization and H_c is the coercivity.

The saturation magnetization and moment per formula unit increased with magnesium concentration from 14.34 emu/g and 0.61 μ_B for x = 0.1 to 42.28 emu/g and 1.66 μ_B for x=0.5 respectively even though the particle size remained the same. This kind of magnetic behaviour may be attributed to controlled doping of site specific cations in the sample. The variation of magnetic parameters in different samples can be understood through either by size effect or by cation distribution. The kind of magnetization observed in our samples with almost uniform particle size as shown in Table 2, supports dominant role of cationic distributions in magnetization over size/surface effects [19]. It is reported that the magnetic behaviour in spinel ferrites depends on the distribution of cations at A and B sites, superexchange interaction and the non-collinear nature of moments at B site. There are three kind of superexchange interactions: intra A-A, B-B and inter sublattice A-B interactions, among which A-B superexchange interaction is the strongest [13]. According to Neel's two sublattice model of ferrimagnetism, the resultant magnetic moment per formula unit is given by

$$M(x) = M_B(x) - M_A(x) \qquad \text{... (6)}$$

where M_B and M_A are the magnetic moments at B and A sites respectively in Bohr magnetons. The Neel's model is modified by Yaffet-Kittel (Y-K) model incorporating the subdivision of B-sublattice into two sublattices having magnetic moments equal in magnitude and each making angle α_{YK} with direction of net magnetization at 0 K. According to Y-K model, the resultant magnetization is expressed as

$$M(x) = M_B \cos\alpha_{YK} - M_A \qquad \text{... (7)}$$

where angle α_{YK} can vary from 0° to 180°. The subdivision occurs when the B-B interaction becomes less stronger than the A-B interaction. In zinc ferrite, which is a normal spinel, the Zn^{2+} and Fe^{3+} ions occupy A and B sites respectively. In this system, Zn^{2+} in A site is diamagnetic, no magnetic moment is expected because the only interaction happening here is B-B superexchange interaction and the B site magnetic moments are antiparallel to each other. The enhancement of magnetization with doping of magnesium which is a B site specific cation is attributed to enhancement of A-B sub lattice interactions by the migration of Fe^{3+} ions from B to A site [20]. It seems that a threshold percentage of Mg is required for initiating the cation distribution in the lattice. All the magnetic parameters remain steady till x = 0.3 beyond which M_s and magnetic moment per formula unit values shoots up supporting Fe^{3+} ions migration from B site to A site and hence enhancing inter sub-lattice A-B superexchange interaction. The coercivity values decreased with magnesium concentration because of its inverse relation with saturation magnetization in accordance with Brown's relation.

In order to determine the magnetic components present in the prepared nanoparticles, M-H curves were fitted with different combinations of magnetic phases. For all the samples, the best fit was obtained for the combination of paramagnetic, superparamagnetic and ferromagnetic phases Fig 8 using the equation (8).

The first, second and third terms in the equation represents ferromagnetism, superparamagnetism and paramagnetism respectively, where M is the magnetization, M^S_F is the saturation magnetization of ferromagnetic component, H_c is the coercivity, S is the squareness ratio, M^s_{sp} is the saturation magnetization of the superparamagnetic component, μ is the magnetic moment per particle, H is the applied field, k is the Boltzmann constant, T is the temperature in Kelvin and χ is the paramagnetic susceptibility. The ferromagnetism in the nanoparticles is evolved from A-B superexchange interaction. The magnetic particles smaller than critical diameter exibit superparamagnetism and paramagnetism arise from the surface spin disorder of the nanoparticles. Thus, the fitting of the M-H data revealed coexistence of ferromagnetic, superparamagnetic and paramagnetic phases in the nanoparticles

$$M = \frac{2M_F^s}{\Pi}\tan^{-1}\left[\left(\frac{H \pm H_c}{H_c}\right)\tan\left(\frac{\Pi S}{2}\right)\right] + M_{sp}^s\left[\cot\left(\frac{\mu H}{kT}\right) - \left(\frac{\mu H}{kT}\right)^{-1}\right] + \chi H \qquad \text{... (8)}$$

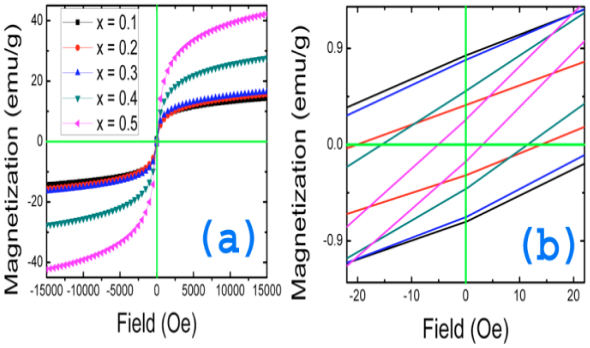

Figure 6. M versus H curves $Mg_xZn_{1-x}Fe_2O_4$ nanoparticles at room temperature. Inset shows magnificent of magnetic hysteresis at low fields

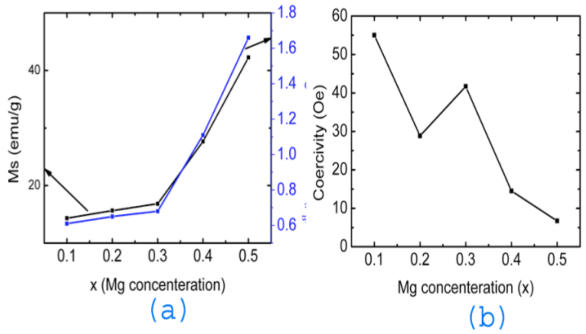

Figure7. Dependence of (a) saturation magnetization, magnetic moment and (b) coercivity

Table 3. Magnetic parameters of $Mg_xZn_{1-x}Fe_2O_4$ nanoparticles

Mg content (x)	Saturation Magnetization Ms (emu/g)	Coercivity H_c (Oe)	Retentivity Mr (emu/g)	magnetic moment (μB)	Squareness ratio (Mr/Ms)	Anisotropy Constant K1 (erg/cm³)
0.1	14.34	55.010	0.7688	0.61	0.0536	2057.810
0.2	15.65	28.838	0.325	0.65	0.0208	1156.913
0.3	16.84	41.705	0.7300	0.68	0.0433	1787.558
0.4	27.66	14.497	0.4536	1.11	0.0164	1009.170
0.5	42.27	6.721	0.1865	1.66	0.0044	702.977

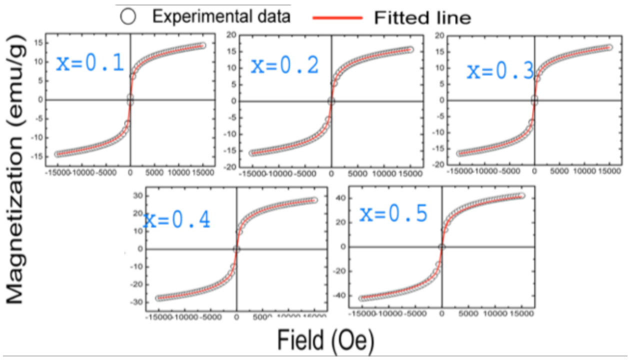

Figure 8. Fitting of M-H data of $Mg_xZn_{1-x}Fe_2O_4$ nanoparticles using eq.(8)

3.5. Mossbauer Spectra Analysis

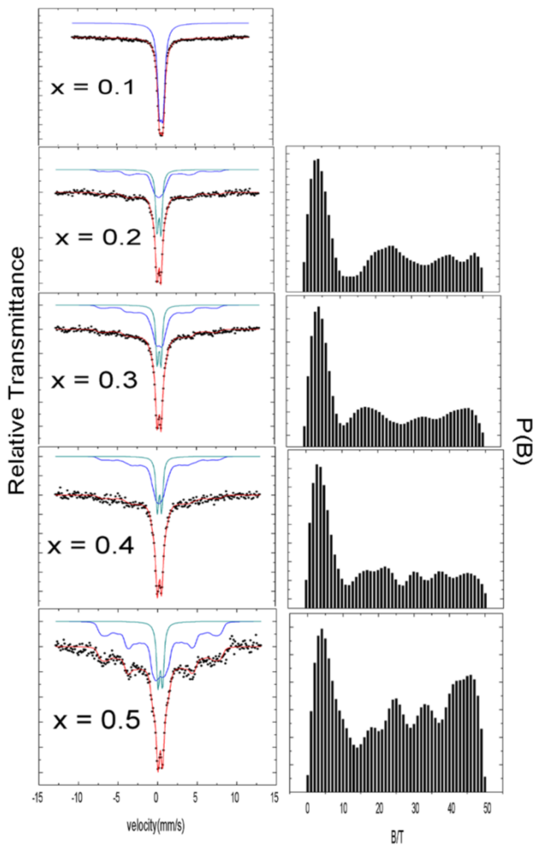

Figure 9. Room temperature Mossbauer spectra of $Mg_xZn_{1-x}Fe_2O_4$ samples with different Mg content. Black dots (•) are the experimental data, red lines represent the best fit, blue and green lines are the subspectra used for fitting. Corresponding distribution of hyperfine field P(Bhf) of respective fractions is given on the right side.

The Mossbauer spectra of the nanoparticles were recorded at room temperature and fitted with Normos/Site and Normos/Dist for discrete sites and distributions respectively. The sample with x = 0.1 is fitted with Normos/Site and others by Normos/Dist as shown in Figure9 along with their distribution of hyperfine fields. In the case of discrete fitting Lorentzian line shape is assumed in all cases. Various hyperfine parameters deduced from Mossbauer spectra, namely isomer shifts (IS), quadrupole splitting (QS), line widths (Γ), average hyperfine fields <H(T)> and relative areas the fitted doublets and distribution are listed in Table 4.

For a magnetic nanoparticle, magnetization direction fluctuates spontaneously with a relaxation time (τ). Above blocking temperature, the relaxation time $\tau << \tau_s$ (where τ_s is the Mossbauer measurement time) and the internal magnetic field at the nucleus is averaged out giving rise to a quadrupolar doublet in the Mossbauer pattern. Below the blocking temperature, $\tau >> \tau_s$, a sextet Mossbauer pattern is observed and near the blocking temperature when $\tau \sim \tau_s$, a partially collapsed sextet with broad lines are seen [21]. Mossbauer spectra of all fractions exhibited simultaneous presence of a central superpararamagnetic / paramagnetic doublet superposed on a weak single magnetic sextet except in one sample(x = 0.1). The Mossbauer spectrum of the low Mg fraction(x = 0.1) closely resembled $ZnFe_2O_4$ with single superparamagnetic / paramagnetic doublet. Unlike other reported results [22], IS value of the doublet is greater than 0.5(Table 4) indicating that most of the Fe^{3+} ions occupy octahedral sites in their high spin state since the presence of Fe^{2+} is not a possibility of the sample prepared using a polymer precursor annealed at and around 450˚C[23]. For fractions x = 0.2, 0.3, 0.4 and 0.5 we could fit spectra only by considering hyperfine magnetic field distributions. The results revealed their superparamagnetic / paramagnetic (strong single doublet) and weak magnetic ordering (a less intense sextet). The broad sextet and broad magnetic hyperfine field distribution P(Bhf) in Fig 9 is due to the variation of A-B interaction from region to region [24]. In these fractions, intensity of sextet increases with the concentration of Mg^{2+} ions and this trend is reported by many researchers [21], [24]–[29]. As in the Table 4 the relative area of distribution increased with Mg content and the average magnetic hyperfine field changed from 17.6 T for x = 0.2 to 24.77 T for x = 0.5. These findings can be explained by the enhancement of A-B superexchange interaction strength due to the redistribution of Fe^{3+} ions among tetrahedral and octahedral sites (Table 1)[26]. In general, hyperfine field at the B site decreases with Zn concentration in A sites according to the relation

$$H_n = H_o(1 - n\Delta H) \qquad \dots (10)$$

where H_o is the field at B site with no Zn ion in A site, n is the number of Zn ions in A sites and ΔH is the fractional decrease in hyperfine field[30]. The Mossbauer spectra for x > 0.1 are consistent with the formation of a fairly good solid solution as local inhomogeneous clusters with a central doublet characteristic of particles undergoing SPM relaxation or having paramagnetic character and an emerging sextet attributable to bigger ferrite particles with their relaxation time approximately is of the order of the characteristic Mossbauer measurement time. Probability distribution of hyperfine fields of all the samples have most probable field around 4 T(low field), representing doublets indicated majority of particles are undergoing superparamagnetic relaxation. The samples with x = 0.2, 0.4 and 0.4 have only low intense peaks at higher fields (Table 4 , Fig 10) and x = 0.5 has comparatively more intense peaks confirmed the presence of particles that contribute to a relaxation time comparable to measurement time. Thus Mossbauer spectra analysis corroborated the presence of ferromagnetic, superparamagnetic and paramagnetic phases determined by M-H curve fitting. No trace of impurity was detected in the samples.

Table 4. Variation of isomer shift and quadrupole splitting of $Mg_xZn_{1-x}Fe_2O_4$ samples

Mg Content(x)	Sub-spectrum	IS (mm/s)	QS (mm/s)	Γ (mm/s)	Area (%)	<H(T)>	Peak Values of P(Bhf)
0.1	Doublet	0.70	0.45	0.615	100	-	-
0.2	Doublet distribution	0.33 0.32	0.49 -	0.41 0.40	41.97 58.03	- 17.6	- 4.03, 24.52, 40.58, 48.01
0.3	Doublet distribution	0.32 0.34	0.48 -	0.4 0.4	29.82 70.18	- 17.4	4.02, 17.0, 33.57, 46.23
0.4	Doublet distribution	0.32 0.30	0.54 -	0.41 0.39	26.56 73.44	- 17.7	3.17, 22.31, 30.67, 37.51, 45.53
0.5	Doublet distribution	0.34 0.27	0.56 -	0.46 0.4	17.94 82.06	- 24.77	4.02, 18.03, 25.04, 33.42, 46.23

4. Conclusions

$Mg_xZn_{1-x}Fe_2O_4$ nanoparticles were synthesized using spray pyrolysis method and the effect of Mg doping on the structural, magnetic and hyperfine properties were investigated using XRD, FTIR, VSM and Mossbauer spectroscopy. The XRD patterns revealed the cubic spinel structure and structural refinement was done by Rietveld method using FULLPROF program. The cation distribution, lattice parameter and oxygen position parameter were extracted from the Rietveld refinement. The migration of Fe^{3+} ions from octahedral to tetrahedral site with magnesium doping was observed from the cation distribution. The lattice parameter decreased with magnesium concentration obeying Vegard's law owing to comparatively smaller ionic radii of Mg^{2+} than Zn^{2+} and by change in the cations in interstitial sites. The average particle size obtained from TEM image of $Mg_{0.5}Zn_{0.5}Fe_2O_4$ was about 15 nm and majority of particles were spherical. The particle size lies in the range of 9-19 nm with possibility of coexistence of superparamagnetic particles with some bigger particles. The FTIR analysis confirmed spinel structure and center of the υ_1 band in the FTIR spectra shifted to longer wavenumber with Mg doping because of the replacement of Zn^{2+} by Fe^{3+} with comparatively lower atomic weight at the tetrahedral sites. The curve fitting of M-H data revealed the coexistence of superparamagnetic, ferromagnetic and paramagnetic particles. Saturation magnetization and magnetic moment per formula unit were found to increase with Mg doping due to enhancement of A-B superexchange interaction by the redistribution of Fe^{3+} ions among the interstitial sites. The Mossbauer spectrum of the samples except with x = 0.1 is a centerall superparamagnetic doublet superposed on weak single magnetic sextet. The Mossbauer spectra and hyperfine field distribution with most probable field at low field suggest majority of particles are undergoing superparamagnetic relaxation and few are ferromagnetic whose relaxation time equals Mossbauer measurement time. The area of the sextet and mean hyperfine field increased with magnesium concentration owing to increase in the A-B superexchange interaction as in the magnetization data analysis. The Mossbauer analysis strongly confirmed the coexistence of superparamagnetic, ferromagnetic and paramagnetic phases observed in magnetization data fitting by the superposition of a doublet and a collapsed sextet.

Acknowledgements

The authors wish to thank Dr. V R Reddy (UGC-DAE Consortium for Scientific Research, Indore) for the Mossbauer measurements and STIC, Cochin for the TEM and FTIR analysis.

References

[1] H.M. Zaki, A. Umar, T. A. Elmosalami, and H.A. Dawoud, "Magnesium-Zinc Ferrite

Nanoparticles : Effect of Copper Doping on the Structural, Electrical and Magnetic Properties," J. Nanosci. Nanotechnol., vol. 13, pp. 4056–4065, 2013.

[2] H.-C. Wu et al., "Magnetic and transport properties of epitaxial thin film MgFe2O4 grown on MgO (100) by molecular beam epitaxy," Sci. Rep., vol. 4, no. 1, pp. 1–6, 2015.

[3] J. Smit and H. P. J. Wijn, Ferrites. London: Philips' Technical Library, 1959.

[4] V.D. Kassabova-zhetcheva, L.P. Pavlova, B.I. Samuneva, Z. P. Cherkezova-zheleva, I. G. Mitov, and M.T. Mikhov, "Characterization of superparamagnetic $Mg_xZn_{1-x}Fe_2O_4$ powders," Centeral Eur. J. Chem., vol. 5, no. 1, pp. 107–117, 2007.

[5] L.M. Salah, A.M. Moustafa, and I.S.A. Farag, "Structural characteristics and electrical properties of copper doped manganese ferrite," Ceram. Int., vol. 38, no. 7, pp. 5605–5611, 2012.

[6] C. Srinivas et al., "Structural and magnetic characterization of co-precipitated $Ni_xZn_{1-x}Fe_2O_4$ ferrite nanoparticles," J. Magn. Magn. Mater., vol. 407, pp. 135–141, 2016.

[7] F. Luo and C. Yan, "Anti-phase boundaries pinned abnormal positive magnetoresistance in Mg doped nanocrystalline zinc spinel ferrite," Chem. Phys. Lett., vol. 452, pp. 296–300, 2008.

[8] L. J. Berchmans, R. K. Selvan, P. N. S. Kumar, and C.O. Augustin, "Structural and electrical properties of $Ni_{1Ax}Mg_xFe_2O_4$ synthesized by citrate gel process," J. Magn. Magn. Mater., vol. 279, pp. 103–110, 2004.

[9] S. D. Chhaya, M. P. Pandya, M. C. Chhantbar, K. B. Modi, G. J. Baldha, and H. H. Joshi, "Study of substitution limit, structural, bulk magnetic and electrical properties of Ca^{2+} substituted magnesium ferrite," J. Alloys Compd., vol. 377, pp. 155–161, 2004.

[10] V. B. Kawade, G. K. Bichile, and K. M. Jadhav, "X-ray and infrared studies of chromium substituted magnesium ferrite," Mater. Lett., vol. 42, no. 1, pp. 33–37, 2000.

[11] M. V Limaye et al., "High Coercivity of Oleic Acid Capped $CoFe_2O_4$ Nanoparticles at Room Temperature," J. Phys. Chem. B, vol. 113, pp. 9070–9076, 2009.

[12] A. Gholizadeh and E. Jafari, "Effects of sintering atmosphere and temperature on structural and magnetic properties of Ni-Cu-Zn ferrite nanoparticles: Magnetic enhancement by a reducing atmosphere," J. Magn. Magn. Mater., vol. 422, pp. 328–336, 2017.

[13] H. Sozeri, Z. Durmus, and A. Baykal, "Structural and magnetic properties of triethylene glycol stabilized $Zn_xCo_{1A_x}Fe_2O_4$ nanoparticles," Mater. Res. Bull., vol. 47, no. 9, pp. 2442–2448, 2012.

[14] H. Wu, T. Li, L. Xia, and X. Zhang, "Microwave-polyol controlled synthesis and magnetic properties of monodisperse Co x Ni 1 A x Fe 2 O 4 / MWCNT nanocomposites," Mater. Res. Bull., vol. 48, no. 11, pp. 4785–4790, 2013.

[15] A. Baykal, F. Gözüak, H. Kavas, and Y. Köseog, "Structural and magnetic properties of $Co_xZn_{1Ax}Fe_2O_4$ nanocrystals synthesized by microwave method," Polyhedron, vol. 28, pp. 2887–2892, 2009.

[16] V. Jagadeesha Angadi, A. V. Anupama, R. Kumar, S. Matteppanavar, B. Rudraswamy, and B. Sahoo, "Observation of enhanced magnetic pinning in Sm3+ substituted nanocrystalline Mn-Zn ferrites prepared by propellant chemistry route," J. Alloys Compd., vol. 682, pp. 263–274, 2016.

[17] F. Gozuak, Y. Koseoglu, A. Baykal, and H. Kavas, "Synthesis and characterization of

$Co_xZn_1A_xFe_2O_4$ magnetic nanoparticles via a PEG-assisted route," J. Magn. Magn. Mater., vol. 321, pp. 2170–2177, 2009.

[18] A.A. Ati, Z. Othaman, and A. Samavati, "Influence of cobalt on structural and magnetic properties of nickel ferrite nanoparticles," J. Mol. Struct., vol. 1052, pp. 177–182, 2013.

[19] T. Zaki, K. I. Kabel, and H. Hassan, "Using modified Pechini method to synthesize α-Al2O3 nanoparticles of high surface area," Ceram. Int., vol. 38, no. 6, pp. 4861–4866, 2012.

[20] H. Wu, N. Zhang, L. Mao, T. Li, and L. Xia, "Controlled synthesis and magnetic properties of monodisperse Ni 1 A x Zn x Fe 2 O 4 / MWCNT nanocomposites via microwave-assisted polyol process," J. Alloys Compd., vol. 554, pp. 132–137, 2013.

[21] B. K. Nath, P. K. Chakrabarti, S. Das, U. Kumar, P. K. Mukhopadhyay, and D. Das, "P HYSICAL J OURNAL B M ¨ ossbauer , X-ray diffraction and AC susceptibility studies on nanoparticles of zinc substituted magnesium ferrite," EUOROPEAN Phys. J. B, vol. 425, pp. 417–425, 2004.

[22] M. A. Ã. Gabal, "Effect of Mg substitution on the magnetic properties of NiCuZn ferrite nanoparticles prepared through a novel method using egg white," J. Magn. Magn. Mater., vol. 321, no. 19, pp. 3144–3148, 2009.

[23] V. Sepelak, M. Menzel, K. D. Becker, and F. Krumeich, "Mechanochemical reduction of magnesium ferrite," J. Phys. Chem. B, vol. 106, no. 26, pp. 6672–6678, 2002.

[24] V. Jagadeesha Angadi et al., "Dose dependent modifications in structural and magnetic properties of γ-irradiated nanocrystalline Mn0.5Zn0.5Fe2O4 ceramics," Ceram. Int., vol. 43, no. 1, pp. 523–526, 2017.

[25] H. Spiers et al., "Self propagating high temperature synthesis of magnesium zinc ferrites ($Mg_xZn_{12x}Fe_2O_3$): thermal imaging and time resolved X-ray diffraction experiments {," J. Mater. Chem., vol. 14, pp. 1104–1111, 2004.

[26] F. Nakagomi, M. S. Silva, A. F. Jr, V. K. Garg, A. C. Oliveira, and P. C. Morais, "Raman study of cations' distribution in $Zn_xMg_{12x}Fe_2O_4$ nanoparticles," J. Nanoparticle Res., vol. 14, no. 798, pp. 1–10, 2012.

[27] M.E. Abbasher M Gismelseed, K.A.Mohammed, HM Widatallah, A D Al-Rawas and E. and A. A. Yousif, "Structure and magnetic properties of the $Zn_xMg_{1-x}Fe_2O_4$ ferrites," in International Conference on the Applications of the Mössbauer Effect (ICAME 2009), 2009, vol. 217, pp. 1–4.

[28] M.A. Gabal and Y.M. Al Angari, "Effect of diamagnetic substitution on the structural, magnetic and electrical properties of $NiFe_2O_4$," Mater. Chem. Phys., vol. 115, no. 2–3, pp. 578–584, 2009.

[29] S.M. Attia, "Study of Cation Distribution of Mn-Zn Ferrites," Egypt. J. Solids, vol. 4, no. 29, pp. 329–340, 2006.

[30] C.S. Kim, W.C. Kim, S.Y. An and S.W. Lee, "Structure and Mössbauer studies of Cu-doped Ni–Zn ferrite," J. Magn. Magn. Mater., vol. 215, pp. 213–216, 2000.